scientific reports

Check for updates

OPEN

The lithological characteristics of natural gas hydrates in permafrost on the Qinghai of China

Da Lei[1,2,3,4]✉, Changmin Fu[1,2,3,4], Qihui Zhen[1,2,3], Zhongxing Wang[1,2,3,4] & Ruo Wang[1,2,3,4]

The environment is seriously threatened by the methane emitted as permafrost melts. Studying deposits of natural gas hydrates that include methane is therefore important. This study presents a novel approach based on the rock Archie formula to discover the porosity and saturation of gas hydrates. The relationship between resistivity and porosity and the porosity of hydrates was studied, and the results showed that the resistivity of hydrate reservoirs was closely related to porosity and hydrate saturation, and the polarization rate was only related to the concentration of natural gas hydrates and had nothing to do with porosity. Using the multi-channel time domain induced polarization (MTIP) method, the profile with five boreholes in the Muli area of the permafrost area of the Qinghai-Tibet Plateau was observed, and the thickness of the shallow permafrost distribution and the underground structure were inferred based on the resistivity of the MTIP data. The polarization rate and hydrate saturation of the inversion assessed the presence of hydrates in the Muli region. The results show that the MTIP method can be used to detect the thickness of permafrost distribution, determine fault boundaries, reveal the distribution of natural gas transport paths, and evaluate the presence of natural gas hydrates.

Gas hydrates are crystalline minerals that are made up of water and various gases. They are discovered in large quantities, mainly on the seafloor and in regions with permafrost[1,2]. Hydrates are a source of combustible energy. Estimated global reserves are 2.1×10^{15} m^3, twice the total reserves of coal, oil, and natural gas combined[3,4]. Therefore, countries all over the world, especially developed countries and those with energy shortages, have attached great importance to research on natural gas hydrates (NGH). The United States, Japan, Germany, India, and Canada have established institutes to research NGH as well as development plans to expedite the exploration, development, and utilization of their resources. Based on research in these countries, nine permafrost regions containing NGH have been identified. They are located in Russia, the United States, Canada, and countries in the permafrost zone of the Central Arctic[5]. China has the third largest permafrost deposits of NGH in the world, which are on the Qinghai-Tibetan Plateau and the Greater Xingan Mountains, accounting for approximately 22.3% of China's reserves[6]. The permafrost region of Qilian Mountain, China, is located on the northern edge of the Qinghai-Tibet Plateau and is primarily composed of mountain permafrost. The average annual surface temperature of the continuous permafrost area is − 2 to − 2.5 °C, and the frozen soil layer thickness is 60–95 m[6]. It can provide advantageous temperature and pressure conditions as well as an excellent trap effect for the formation of NGH.

In marine surveys, seismic techniques have been used to locate NGH in sediment under the stable zone of the seabed[7–24]. Seismic methods are used to predict the amount of methane in the saturated hydrate in the pore space of NGH reservoirs[25–31]. The controlled-source electromagnetic method has been used to determine the pore saturation[30–32]. The seismic reflection method has proven to be effective against NGH exploration in permafrost[33,34], whereas electromagnetic methods have only recently been used in the field to study hydrate deposits[35,36].

[1]CAS Engineering Laboratory for Deep Resources Equipment and Technology, Institute of Geology and Geophysics, Chinese Academy of Sciences, Beijing 100029, China. [2]Institute of Geology and Geophysics, Chinese Academy of Sciences, Beijing 100029, China. [3]College of Earth and Planetary Sciences, University of Chinese Academy of Sciences, Beijing 100049, China. [4]Innovation Academy for Earth Science, Chinese Academy of Sciences, Beijing 100029, China. ✉email: leida@mail.iggcas.ac.cn

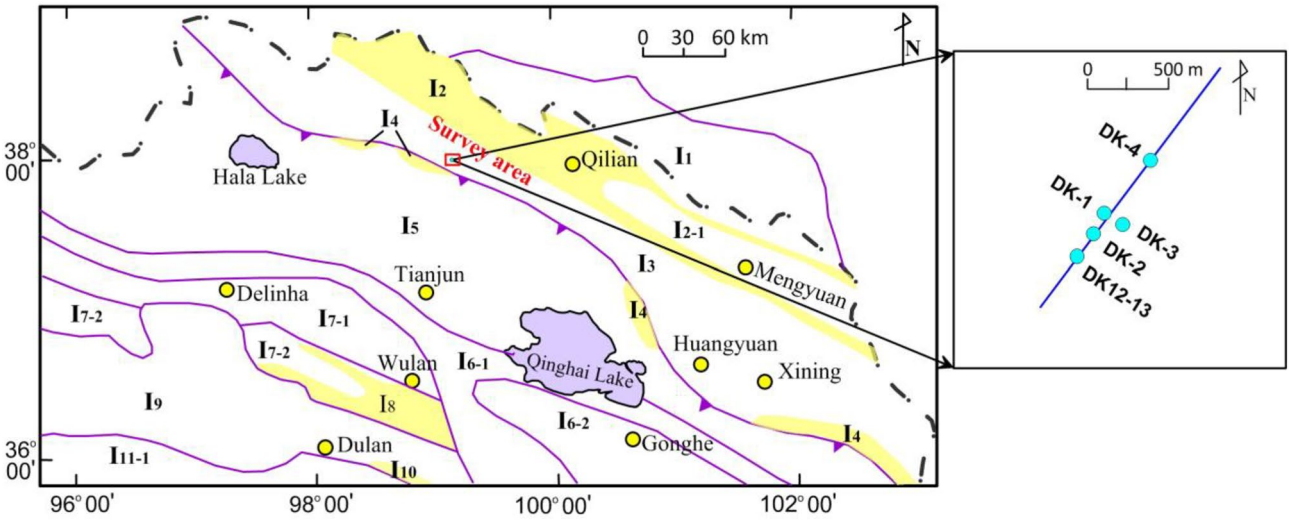

Figure 1. Schematic diagram of structures within the study area overlaid on an aerial photograph. I_1 represents the Alxa landmass; I_2 represents the Northern Qilian neo-Proterozoic to early Paleozoic suture zone. $I_{2\text{-}1}$ represents the Qilian-Menyuan magmatic arc zone, middle and late early Paleozoic (O-S). I_3 represents the Qilian block in the center. I_4 represents the Suture zone between Shule Nanshan and Laguiyama in the Early Paleozoic. I_5 represents the Southern Qilian's landmass. I_6 represents the Late Paleozoic-Early Mesozoic Fracture Trough (D-T2) at ZongwuLongshan-Qinghai Nanshan. $I_{6\text{-}1}$ represents the Zongwu Longshan-Xinghai Aola Trough (D-P). $I_{6\text{-}2}$ represents the Post-Foreland Basin of the Zeku Arc ($T_{1\text{-}2}$). I_7 represents the Oulongbrook Land Block. $I_{7\text{-}1}$ represents the Orbo Mountain, Craton Edge Basin. $I_{7\text{-}2}$: T-shaped VI-Amunik Mountain-Depleted Late Neoproterozoic Niushan Magma Arc Belt (Pt_3-S). I_8 represents the ChaiBei Rim's Suture Zone. I_9 represents the Qaidam's Plot. I_{10} represents the Qimantag-Dulan Suture Zone. I_{11} represents the Dongkun Middle Land Block. $I_{11\text{-}1}$ represents the Dongkun Middle Magma Arc Zone (Pt_3-J). The blue dots in the box on the right represent the drilling wells within the survey area (Modified from Lu et al.[7], 2010. Map created in Surfer 14.0.599 of Golden Software, LLC (https://www.goldensoftware.com/products/surfer).

In recent decades, the China Geological Survey Bureau has supported research on NGH in permafrost regions. In 2008 and 2009, research was carried out in the permafrost region of the Qilian Mountains along the northern edge of the Qinghai-Tibetan Plateau, which has conditions suitable for NGH. An NGH Scientific Drilling Project was carried out in the Qilian Mountains. Boreholes DK-1, DK-2, DK-3, DK-4, and DK12-13 were drilled, and sufficient rock samples of gas hydrates were obtained to give rise to scientific and economic importance[37,38]. An electromagnetic method[39] has been used for NGH exploration in China since 2009. We have further evaluated hydrates in a typical section in the Qilian Mountains Muli region using multichannel time-domain induced polarization (MTIP) to determine the distribution of permafrost, source rocks, and transport channels of hydrates, as well as the distribution of hydrates delineated according to polarizability and NGH saturation, providing methodological support for an in-depth understanding of the distribution pattern and resource potential of gas hydrates in the area.

Study area

Geological background. According to[40], the Qilian Mountains are in the northeast of the Qinghai–Tibet Plateau, China. There are three major tectonic units: the north Qilian tectonic belt (Hexi corridor and South Mountain corridor), the middle Qilian continental block (Tolai Mountain), and the south Qilian tectonic belt, which correspond to I2, I3, and I5 in Fig. 1, respectively. The main body of the southern Qilian tectonic belt is a superposed basin from the late Paleozoic to the Mesozoic, which developed by early Paleozoic tectonic evolution.

Boreholes DK-1, DK-2, and DK-3 were drilled in the town of Tianjun in Qinghai Province, in the permafrost regions of Muli, which are at an elevation of between 4026 and 4128 m. The three holes revealed a permafrost thickness of approximately 95 m[41] and an average annual surface temperature of approximately − 2 to − 2.5 °C in the area, with the main drilling area being in the South Qilian structural belt, which is subordinate to the Muli Depression[42,43].

The central part of the study area is composed of anticlinal Triassic strata, and in the north and south, there are two synclinal Jurassic coal-bearing strata. The large-scale thrust nodes on the north and south of the anticline control the boundary of the depression. The north–south synclines have caused a series of large shear faults in the northeast that cut the depression into intermittent segments of different sizes (Fig. 1). The boreholes reveal that strata within the study region contain the Jurassic Jiangcang Formation (J_2j) and Muli Formation (J_2m), but not the Quaternary system. The Muli Formation roughly corresponds to the Xiangtang Formation (J_2x) and the Yaojie Formation (J_2y) in this region.

Lu et al.[40] claim that there are several recoverable coal seams in the strata mentioned above. The Jiangcang Formation (J_{2j}) is dominated by black and gray oil shale, mudstone, gray sandstone, and fine sandstone. The

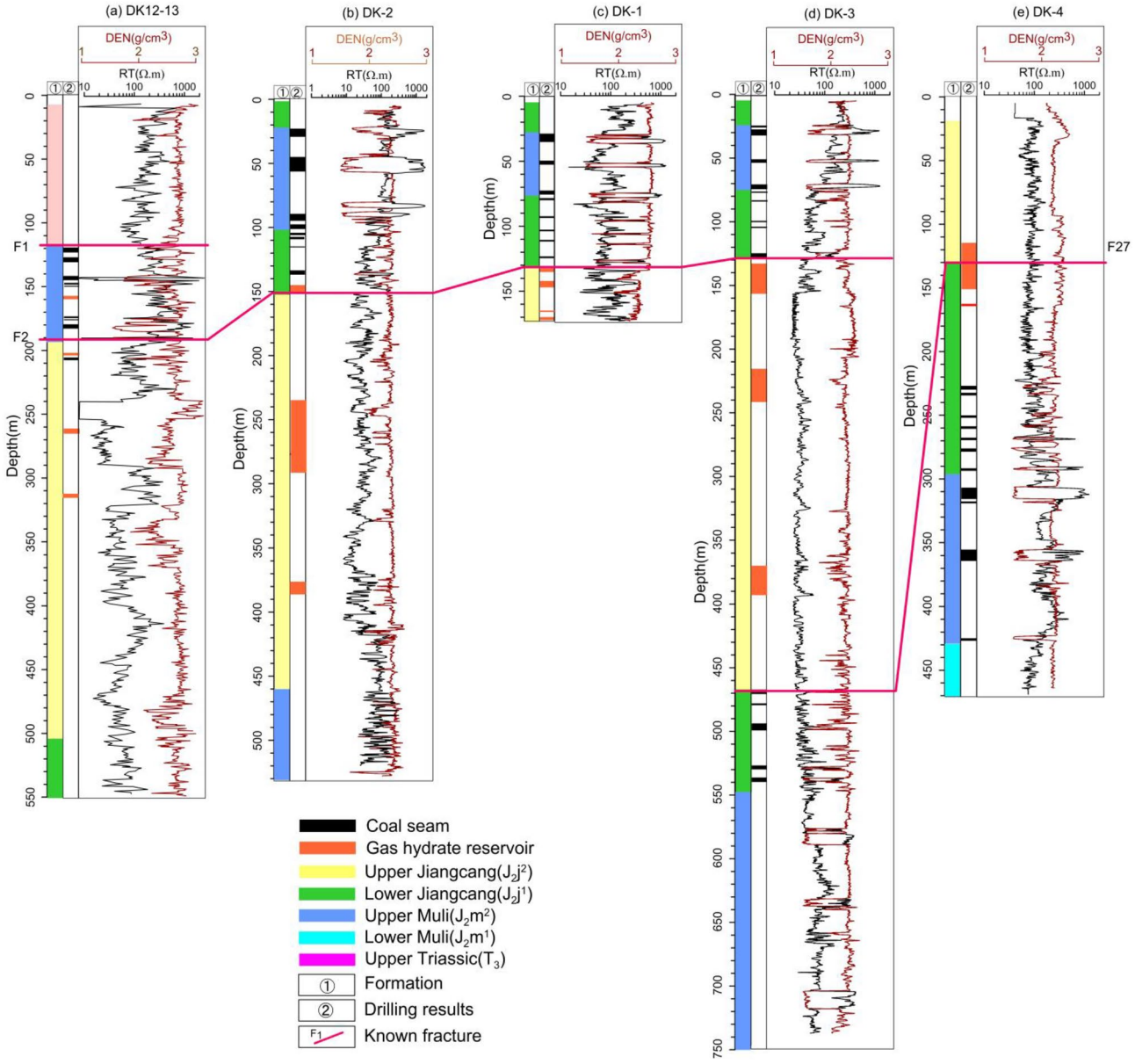

Figure 2. Resistivity versus depth from well logs: (**a**) DK12-13, (**b**) DK-2, (**c**) DK-1, (**d**) DK-3, and (**e**) DK-4.

Muli Formation (J_2m) is dominated by gray and gray-white siltstone, fine sandstone, medium sandstone, coarse sandstone (gravel), deep gray mudstone, and oil shale, which are sediment from a braided river delta and the main coal-bearing section. It contains two major coal seams and several local thin coal seams. However, the hydrate is mainly distributed in the mudstone, siltstone, oil shale, and fine sandstone. It is between 130 and 400 m deep in rock fractures that may not be visible to the naked eye. It appears as an abnormality in finely disseminated deposits distributed in rock pores. These strata belong to the Jiangcang Formation.

Electrical and lithological characteristics of NGH. The MTIP survey carried out in the permafrost region of the Qilian Mountains was based on differences in resistivity between the targeted geological bodies (e.g., permafrost and structural faults) and the surrounding rocks. Gas hydrates occur in fissures of siltstone, mudstone, oil shale, or in pores of sandstone. The content of organic carbon in the oil shale is 0.98–5.76%, which satisfies the standard for high-quality source rock[44]. Oil shale has entered its mature period and is the main source of gas[40,45].

NGH is unstable under normal temperatures and pressure, and thus, it is difficult to determine its physical characteristics by collecting samples. However, it is not difficult to analyze the characteristics of the resistivity of NGH and permafrost using in-situ measurements from well logging. An analysis of log data from this area revealed that the NGH and permafrost have a higher resistivity than the normal sedimentary strata.

Figure 2a–e, respectively, show the logs of borehole resistivity from wells DK12–13, DK–2, DK–1, DK–3, and DK–4 in the Qilian Mountains. The figures demonstrate that the resistivity of layers of sandstone, shale,

Borehole	Reservoir lithology	Gas hydrate bearing layers (m)	Resistivity value of surrounding rock (Ω m)	Reservoir resistivity value (Ω m)
DK-1	133.5–135.5	Sandstone	53.85–61.90	203.73–378.41
	142.7–147.7	Siltstone	52.85–88.05	146.41–349.92
	165.45–166.55	Siltstone	30.44–34.21	49.48–96.99
	169.0–170.5	Siltstone	55.98–76.96	101.94–242.12
DK-2	144.40–156.6	Shaly sand	19.42–64.39	28.39–182.73
	275.8–277.1	Siltstone	29.55–36.69	45.75–70.08
	282.5–283.7	Mudstone, siltstone and oil shale	46.08–56.70	78.22–98.93
DK-3	133.0–156.0	Mudstone, siltstone and oil shale	25.67–30.72	40.29–86.16
	225.1–240.0	Mudstone	29.86–35.5	25.37–47.95
	367.7–396.0	Mudstone	24.87–27.91	24.17–59.64
DK-4	115.0–150.0	Siltstone, mudstone	70.16–77.54	57.87–153.70
	162.0–163.0	Siltstone, mudstone	59.71–61.51	66.44–84.22
DK12-13	157.5–160.3	Siltstone	91.11–210.21	260.3–396.6
	201.3–203.5	Shaly sand	37.3–56.4	80.19–170.12
	263.2–265.4	Mudstone	12.17–20.21	30.03–55.89
	314.0–316.1	Siltstone	120.02–183.67	200.89–300.51

Table 1. Statistics of resistivity values of NGH Reservoirs from resistivity logging.

siltstone, oil shale, and mudstone, within which the NGH was mainly deposited, ranged from 133 to 283.7 m, and from 314 to 396 m, respectively.

The gas hydrate-bearing layers show obvious high resistivity anomalies in the resistivity logs of DK-1 and DK12–13, while other log resistivity curves have weaker displays. According to the lithological characteristics of five well logs, the resistivity values of hydrate-bearing layers are statistically classified in Table 1. It can be seen in Table 1 that NGH revealed by well DK-1 exists in sandstone and siltstone. The mean resistivity value of the hydrate gas-bearing layers is 3.35 times higher than that of the surrounding rock. The NGH revealed by well DK12-13 exists in siltstone, shale, and mudstone, and the mean resistivity value of the gas hydrate-bearing layers is 2.30 times higher than that of the surrounding rock. The NGH revealed by wells DK-2, DK-3, and DK-4 exists in mudstone, siltstone, and oil shale, and the mean resistivity value of the gas hydrate-bearing layers is 1.70 times higher than that of the surrounding rock. The mean resistivity value of the NGH layers in five holes is 2.26 times higher than that of the surrounding rock. It is consistent with the conclusion pointed out by Fang et al.[39] that the resistivity of the gas hydrate layer is two to three times higher than that of the surrounding rock.

Comprehensive information from the drilling and cores shows that the NGH mainly occurs in the Jiangcang formation in the Middle Jurassic of the Muli permafrost.

In well DK-1, porosity measurements from core samples of the four wells ranged from 5 to 20%. The range of NGH saturation obtained by the Archie equation is 13–86%[46,47]. In wells DK-2 and DK-3, the mean value of NGH saturation obtained by the Archie equation is 9.5% and 15.5%, respectively[48]. Well DK12-13, the range of NGH saturation achieved by the Archie equation is 13–85%[49]. Therefore, the porosity of the rocks in the four wells varied from 5 to 20%, and the saturation varied from 13 to 86%.

The reservoir resistivity range of the gas hydrate-bearing layers is the minimum and maximum values of the corresponding logging resistivity curves, and the surrounding rock resistivity range is the minimum and maximum values of the logging resistivity curves corresponding to the upper and lower formations of NHG-bearing reservoirs.

MTIP sounding layout. An experimental study of the MTIP sounding method for the detection of NGH has been ongoing in the Muli area since 2008. The survey lines are shown in Fig. 3. Line 3 was across wells DK-4, DK-3, and other gas hydrate investigation wells, which were 2100 m long. In the pole–dipole setup, the dipole spacing was used at 20 m.

Methods

The MTIP principle. MTIP is an array exploration method based on the difference between in conductivity and polarizability between the study object and the surrounding rock and the distribution of the conduction current underground under the action of an artificially stabilizing current field[50]. The survey diagram is shown in Fig. 4. It is a time-domain-induced polarization method. As with conventional ECR with polarization, all receiving electrodes and receiving wires on a profile are laid out prior to measurement, and pole-dipole devices are used for observation. However, the difference is that our team's multi-purpose GDP electrical system (Zonge Ltd., USA) It was developed to be used with an 8-channel transfer switch developed to observe the data through the transfer switch. This allows the use of GDP's high-power transmitter and high-precision data acquisition device for deep apparent resistivity and polarization measurements. The distance between the measuring points and the electric dipole moment can be flexibly varied depending on the depth. Therefore, MTIP resistivity and polarizability imaging is a detection method with large depths (10–800 m).

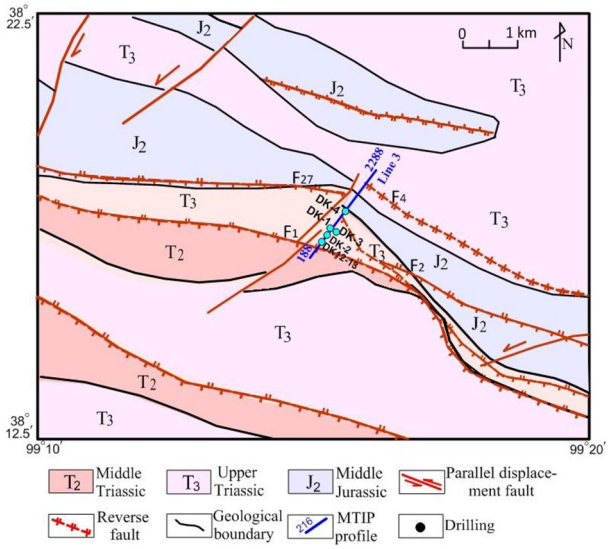

Figure 3. Geological map of the research area; positions of MTIP survey lines; with MTIP sounding profile (blue). Map created in Surfer 14.0.599 of Golden Software, LLC (https://www.goldensoftware.com/products/surfer).

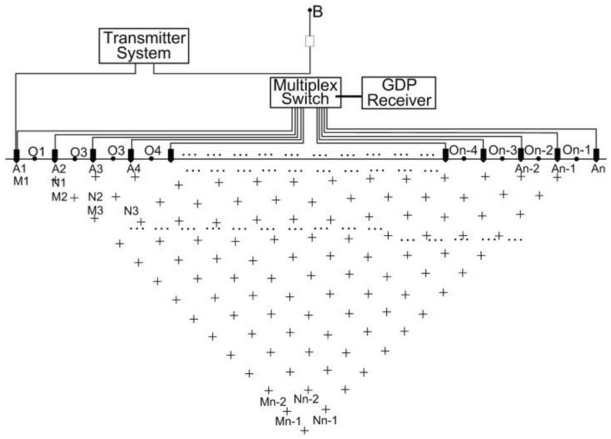

Figure 4. Setup of the MTIP survey.

MTIP data processing. The 2D inversion software TS2DIP 4.40b (Zonge Engineering & Research Organization, Inc., USA. https://zonge.com.au/what-we-do/data-processing) was used for MTIP data inversion. A smoothing model inversion is a robust way to convert resistivity and polarizability data into a smoothly varying model profile. The finite element forward-modeling algorithm used in TS2DIP calculates the apparent resistivity and polarizability with an accuracy of 5% from a 2D model. When information about the terrain is included in the model, the terrain is clearly reflected in the finite element mesh of TS2DIP. Average values of the apparent resistivity and polarizability were calculated and used in the initial background resistivity model. The interactive tool allows the user to edit the background model autonomously based on known geological information. The iterative modification of the 2D model was guided by constraints on both its smoothness and the differences between the background model and the inversion model. This method considered many measures, including the RMS error, to measure data misfit, distance from an a priori background model, model roughness, average RMS model-constraint residual, RMS minimization criteria, and the largest changes in the model parameters after each iteration until the calculated resistivity and polarizability matched the observed data as closely as possible.

Porosity and saturation calculation methodology. In order to use MTIP to explore the NGH in the Muli area of the Qinhai-Tibetan Plateau, it was necessary to study the lithological characteristics based on resistivity and polarizability.

The physical parameters affecting the electrical properties of rocks in the area containing NGH are the porosity and saturation of the gas hydrate. Archie's equation[51] is commonly used to evaluate a reservoir and can be applied to NGH:

$$\rho_t = \frac{a\rho_w}{\phi^m S_w^n}, \tag{1}$$

where ρ_t is the resistivity of the formation (Ω m), ρ_w is the resistivity of the water in the formation (Ω m), and ϕ is the porosity (percentage). It is generally believed that the pores of hydrate-bearing reservoirs contain only hydrates and water, S_w is the saturation of pores in the formation due to water and gas hydrate saturation S_h is obtained by:

$$S_h = 1 - S_w \tag{2}$$

The parameters a, m, and n are empirical indices that can be determined for the stratum. In general, $1.5 < m < 3$, $0.5 < a < 2.5$, and $1.86 < n < 2.06$[46].

According to past research on NGH reservoirs[46,52], $\rho_w = 2$ Ω m, $n = 1.9386$, $a = 0.51$, and $m = 1.32$, so Eq. (1) can be written as

$$\rho_t = \frac{1.02}{\varphi^{1.32}(1 - S_h)^{1.9386}} \tag{3}$$

Equation (3) shows that the resistivity of a NGH reservoir is a function of the porosity and saturation of the NGH. Thus, the resistivity of the NGH reservoir can be deduced from these two parameters in the study area.

In the time-domain IP method, the measured voltage in the rock and ore increased over time with a stable current, indicating that the resistivity of the rock and ore or NGH changed with supply time. In other words, the effect of volumetric polarization of the medium is equivalent to the increase in its resistivity when the supplied current is stable. The equivalent resistivity of the IP is given by Seigel[53].

$$\eta = (\rho_t - \rho_0)/\rho_t = 1 - \rho_0/\rho_t = 1 - \frac{\varphi^{1.32}(1 - S_h)^{1.9386}\rho_0}{1.02} \tag{4}$$

where ρ_t is the resistivity of the formation (Ω m), ρ_0 is the resistivity of non-excited electricity generation when the water content is zero, and η is the polarizability (percentage). Therefore, the polarizability can be estimated with Eqs. (3) and (4). The resistivity calculated according to porosity and NGH content is the equivalent resistivity, and the resistivity calculated without the NGH is the resistivity without excitation. Knowing the resistivity and polarization rate, ϕ and S_h can be obtained by solving together with Eqs. (3) and (4).

Results

MTIP sounding results. Figure 5a shows the two-dimensional resistivity inversion section of MTIP data. It reflects the details of these resistivity logs, especially the high-resistivity anomaly (650 Ω m or more) between depths of 0 and 150 m for the section, which is consistent with the resistivity logs of DK-3 and DK-4. The high-resistivity anomaly shows that there was a layer of frozen soil within the shallow part of this section, and the thickness of the point measurement reaction near the boreholes DK-1, DK-2, and DK-3 coincides with the thickness of the known permafrost layer of about 95 m[41]. The resistivity logs of DK12–13, DK-3, and DK-4 indicate the presence of a lower resistivity region between depths of 200 and 590 m, 100 and 600 m, and from 70 to 260 m, respectively. The low resistivity region was also observed in the resistivity section. NGH reservoirs are distributed in this region. NGH in the Muli area mainly occurs in fractures of mudstone or oil shale, which causes the inclined low resistivity zone of inclined mudstone and the middle-high resistivity anomaly of the NGH reservoir. The results show that the section has seven faults: (a) five south-dipping faults (F0, F1, F2, F27, and F3) and two north-dipping faults (F4, and F5), which reflect the low resistivity seen in MTIP data. (b) MTIP data revealed two north-dipping faults (F4 and F5) associated with low resistivity. The results indicate that the F1, F2 and F27 fracture zones control the formation of NGH. This is consistent with geological and drilling findings that F1, F2 and F27 faults are migration channels for NGH and accumulation spaces for NGH. However, it is difficult to distinguish the NGH layers in the two-dimensional MTIP resistivity inversion section. There are two main reasons for these blind spots. First, the NGH layer is small and it is difficult to identify the deposit with the available detection precision. Secondly, the NGH layer is close to the permafrost layer or close to the faults; hence, the difference in resistivity within the region is very small.

Figure 5b shows the two-dimensional polarizability inversion section for MTIP. There are many high-polarizability anomalies in the section. I, II, and III are inferred ranges of NGH reservoirs. There is a correlation between the known ore-bearing sites and the high-polarizability anomaly I between depths of 190 m and 425 m for DK12–13; depths of 145 m and 390 m for DK-2 and DK-3, respectively; and the high-polarizability II between depths of 145 m and 395 m for DK-4. The I and II high polarizability anomalies are located near the F1, F2 and F27 faults. The high-polarizability anomaly III is near the F3 fault.

Porosity and NGH saturation. To investigate the relations between resistivity, porosity, and NGH content, we assumed that porosity varied from 1 to 95% and at NGH saturation from 1 to 95% based on known drilling information. According to the porosity and saturation of the NGH in the permafrost area of Qilian Mountain, the resistivity of the reservoirs can be estimated with Eq. (3), as shown in Fig. 6. For constant NGH saturation, the resistivity of the NGH reservoir reduced as the porosity increased from 1 to 95%. Similarly, when

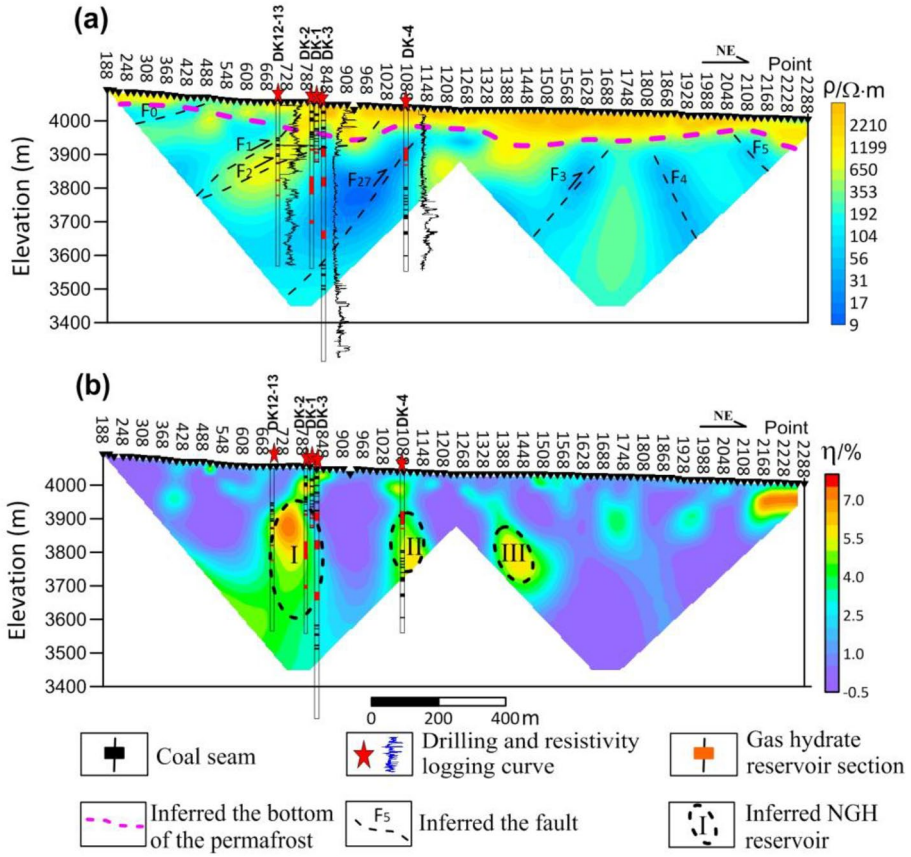

Figure 5. Inferences from well logs and inversion sections of MTIP data. (**a**) Section of two-dimensional inversion resistivity; (**b**) Section of two-dimensional inversion polarizability.

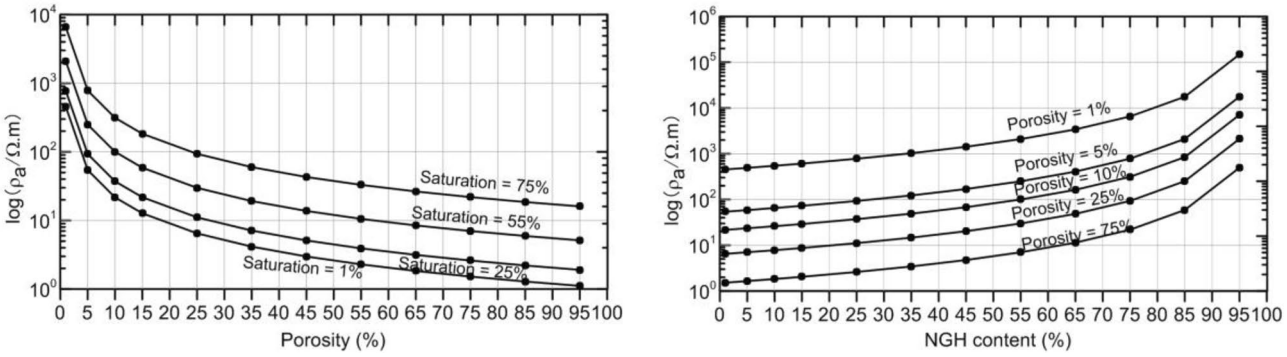

Figure 6. Resistivity as a function of porosity (left) and NGH saturation (right).

the porosity was fixed, the resistivity increased as the NGH saturation increased from 1 to 95%. This indicates that the resistivity of the NGH reservoir is closely related to both porosity and NGH saturation.

It can be seen from Table 1 that the resistivity of the NGH reservoir varies from 24.17 to 396.6 Ω m. It can be found in Fig. 6 that the variation range of porosity and saturation corresponding to this resistivity is 5–20% and 50–70%, respectively.

Figure 6 shows that when the resistivity of the gas hydrate reservoir is higher than 396.6 Ω m, the corresponding porosity will be less than 5% and the saturation will be higher than 70%. It indicates that the reservoir is a low porosity, high saturation reservoir. According to the above analysis, when the porosity is less than 5% and the saturation is higher than 70%, the resistivity parameters of the MTIP method cannot identify and define the NGH reservoirs in the permafrost area of the Qilian Mountains.

The IP can, thus, be calculated, and the polarizability as a function of porosity and as a function of NGH content is shown in Fig. 7. For fixed NGH saturation, the polarizability was constant as the porosity increased from 1 to 95%. However, for a fixed porosity, the polarizability increased as the NGH saturation increased from

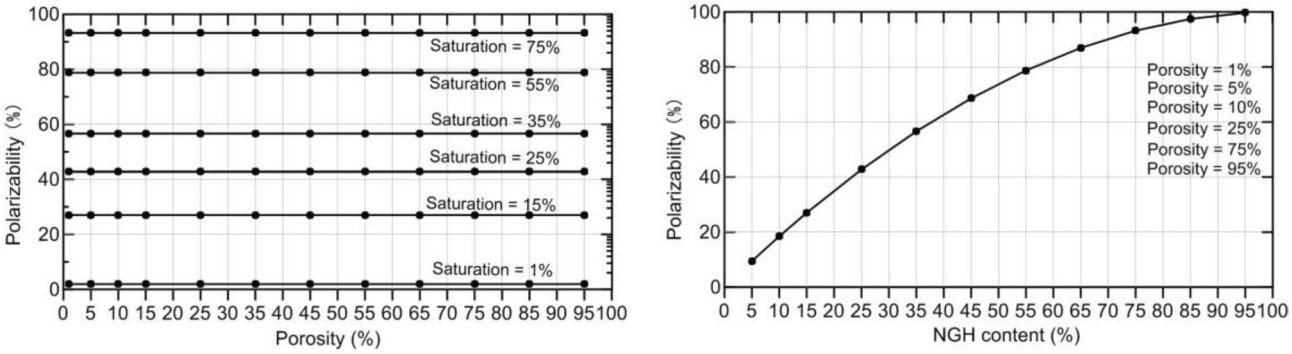

Figure 7. Polarizability as a function of porosity (left) and NGH saturation (right).

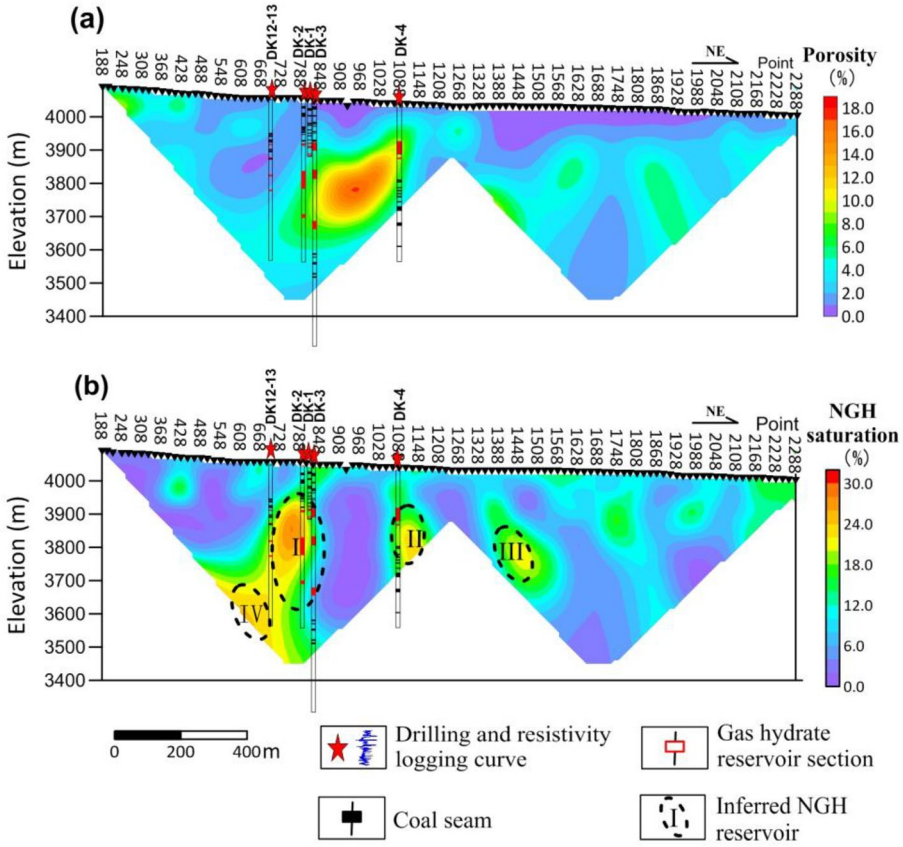

Figure 8. Porosity and NGH saturation sections. (**a**) Section of porosity, (**b**) Section of NGH saturation.

1 to 95%. This indicates that the polarizability depends on the NGH content but not on the porosity. The polarizability, thus, indicates the presence of NGH and can guide the subsequent exploration and drilling.

Based on the ranges of the porosity and saturation of the NGH in the permafrost in the Qilian Mountains, porosity and NGH content can be calculated. The storage capacity of NGH can be found by combining the resistivity and polarizability obtained by MTIP inversion. Hence, based on the difference in polarizability between NGH and the surrounding rock, the polarizability of MTIP is suitable for the geophysical exploration of NGH in the Muli area of the Qinhai-Tibetan Plateau.

The porosity and NGH saturation can be inverted using the MTIP resistivity and polarizability data using Eqs. (3) and (4). The amplitude of the porosity (Fig. 8a) ranges from 0 to 20%. In the shallow permafrost region, the high resistivity corresponds to low porosity, as low as 1%. Faults at elevations between 3700 and 3900 m have a high porosity, up to 20%. The porosity and resistivity distribution reflect the underground lithological characteristics and fault zones. Similarly, NGH saturation (Fig. 8b) ranges from 0 to 32%. The I, II, and III high saturation anomalies are consistent with the I, II, and III high polarizability anomalies. The IV high saturation anomaly is not in the polarizability section.

According to the resistivity and porosity results, as shown in Figs. 5a and 8a, it can be concluded that the fault zone is characterized by a low-resistivity, high-porosity anomaly. The fault zone is characterized by high polarizability and high NGH saturation, as shown in Figs. 5b and 8b. It can be inferred that the NGH in this region depends on the fault zone. The well-developed fracture is a good channel in which NGH can rise, forming NGH in the low-temperature environment due to the layer of permafrost. The fracture can be inferred from the resistivity. When combined with porosity, the degree of fracture development can be determined. The polarization and saturation indicate the presence of NGH.

Conclusions

The electrical and lithological characteristics of gas hydrate reservoirs were studied for use in exploring the presence of NGH in the Muli area, and the presence of NGH in the fault zone was evaluated using the NGH saturation based on MTIP data inversion. The main conclusions are as follows:

1. The porosity of a rock controls its resistivity, and NGH saturation and polarizability are in nice agreement. Three polarizability and saturation anomalies have been recognized as known NGHs, and one saturation anomaly has been identified as a potential NGH. The inferred permafrost overburden thickness and the five south-dipping faults provide a favourable geological environment for hydrate movement and storage.
2. Based on the analysis of the physical properties of underground NGH reservoirs. The resistivity of the sandstone reservoir containing hydrate is 2–3.5 times that of the surrounding rock, and its thickness is thin, so it is difficult to identify the hydrate by resistivity alone, but obtaining resistivity parameters from MTIP can delineate the thickness of the permafrost layer and the fracture distribution to infer the underground NGH source and transport channel.
3. A summary of electrical and lithological characteristics can be used to evaluate the existence of the NGH, The MTIP measurement results are basically consistent with the borehole logging data, and the polarizability and saturation can assess the possibility of the existence of the NGH, which provides an important basis for the identification and distribution of natural gas hydrate reservoirs.

Data availability

Data associated with this research is available and can be obtained by contacting the corresponding author.

Received: 4 May 2022; Accepted: 26 July 2022
Published online: 02 August 2022

References

1. Lee, S. Y. & Holder, G. D. Methane hydrates potential as a future energy source. *Fuel Process. Technol.* **71**(1–3), 181–186 (2001).
2. Zhang, S. L. Study Oil key technology of gas hydrates seismic exploration. *Nat. Gas Ind. (comprehensive study)* **27**(supplement A), 356–370 (2007) (**in Chinese with English abstract**).
3. Kvenvolden, K. A. Methane hydrate—A major reservoir of carbon in the shallow geosphere. *Chem. Geol.* **71**, 41–51 (1988).
4. Makogon, Y. F., Holditch, S. A. & Makogon, T. Y. Natural gas-hydrates—A potential energy source for the 21st century. *J. Petrol. Sci. Eng.* **56**, 14–31 (2007).
5. Dallimore, S. R. & Collett, T. S. Regional gas hydrate occurrences, permafrost conditions, and Cenozoic geology, Mackenzie Delta area. *Geol. Surv. Canada Bull.* **544**, 31–43 (1999).
6. Peng, C. *et al.* Evidence of pore- and fracture-filling gas hydrates from geophysical logs in consolidated rocks of the Muli area, Qinghai-Tibetan Plateau permafrost, China. *J. Geophys. Res. Solid Earth.* **124**, 6297–6314. https://doi.org/10.1029/2018JB016041 (2019).
7. Lu, Z. Q. *et al.* Basic geological characteristics of gas hydrates in Qilian Mountain permafrost area, Qinghai Province. *Mineral Deposits* **29**(1), 182–191 (2010).
8. Yuan, R., Spence, G. D. & Hyndman, R. D. Seismic velocity studies of a gas hydrate bottom-simulating reflector on the northern Cascadia continental margin: Amplitude modeling and full waveform inversion. *Geophys. Res.* **104**(B1), 1179–1191 (1999).
9. Tréhu, A. M. & Flueh, E. R. Estimating the thickness of the free gas zone beneath Hydrate Ridge, Oregon continental margin, from seismic velocities and attenuation. *J. Geophys. Res.* **106**(B2), 2035–2045 (2001).
10. Riedel, M., Spence, G. D., Chapman, N. R. & Hyndman, R. D. Seismic investigations of a vent field associated with gas hydrates, offshore Vancouver Island. *J. Geophys. Res.* **107**(B9), 2200. https://doi.org/10.1029/2001JB000269 (2002).
11. Tréhu, A. M. *et al.* Seismic and seafloor evidence for free gas, gas hydrates, and fluid seeps on the transform margin offshore Cape Mendocino. *J. Geophys. Res.* **108**(B5), 2263. https://doi.org/10.1029/2001JB001679 (2003).
12. Andreassen, K. *et al.* Multicomponent ocean bottom cable data in gas hydrate investigation offshore of Norway. *J. Geophys. Res.* **108**(B8), 2399. https://doi.org/10.1029/2002JB002245 (2003).
13. Depreiter, D., Poort, J., Rensbergen, P. V. & Henriet, J. P. Geophysical evidence of gas hydrates in shallow submarine mud volcanoes on the Moroccan margin. *Geophys. Res.* **110**, B10103. https://doi.org/10.1029/2005JB003622 (2005).
14. Bangs, N. L. B., Musgrave, R. J. & Tre'hu, A. M. Upward shifts in the southern Hydrate Ridge gas hydrate stability zone following postglacial warming, offshore Oregon. *J. Geophys. Res.* **110**, B03102. https://doi.org/10.1029/2004JB003293 (2005).
15. Liu, Y. J., Liu, X. W. & Liu, D. M. Applications of seismic techniques to gas hydrates prediction. *Appl. Geophys.* **5**(1), 67–73 (2008).
16. Priest, J. A., Rees, E. V. L. & Clayton, C. R. I. Influence of gas hydrate morphology on the seismic velocities of sands. *J. Geophys. Res.* **114**, B11205. https://doi.org/10.1029/2009JB006284 (2009).
17. Huang, J. W., Bellefleur, G. & Milkereit, B. Seismic modeling of multidimensional heterogeneity scales of Mallik gas hydrate reservoirs, Northwest Territories of Canada. *J. Geophys. Res.* **114**, B07306. https://doi.org/10.1029/2008JB006172 (2009).
18. Plaza-Faverola, A. *et al.* Evidence from three-dimensional seismic tomography for a substantial accumulation of gas hydrate in a fluid-escape chimney in the Nyegga pockmark field, offshore Norway. *J. Geophys. Res.* **115**, B08104. https://doi.org/10.1029/2009JB007078 (2010).
19. Geletti, R. & Busetti, M. A double bottom simulating reflector in the western Ross Sea, Antarctica. *J. Geophys. Res.* **116**, B04101. https://doi.org/10.1029/2010JB007864 (2011).

20. Jaiswal, P., Dewangan, P., Ramprasad, T. & Zelt, C. A. Seismic characterization of hydrates in faulted, fine-grained sediments of Krishna-Godavari Basin: Full waveform inversion. *J. Geophys. Res.* **117**, B04306. https://doi.org/10.1029/2011JB009024 (2012).
21. Rajan, A., Mienert, J., Bünz, S. & Chand, S. Potential serpentinization, degassing, and gas hydrate formation at a young (<20 Ma) sedimented ocean crust of the Arctic Ocean ridge system. *J. Geophys. Res.* **117**, B03102. https://doi.org/10.1029/2011JB008537 (2012).
22. Sriram, G., Dewangan, P., Ramprasad, T. & Rao, P. R. Anisotropic amplitude variation of the bottom-simulating reflector beneath fracture-filled gas hydrate deposit. *J. Geophys. Res.* **118**, 2258–2274. https://doi.org/10.1002/jgrb.50176 (2013).
23. Crutchley, G. J. *et al.* Gas migration into gas hydrate-bearing sediments on the southern Hikurangi margin of New Zealand. *J. Geophys. Res. Solid Earth.* **120**, 725–743. https://doi.org/10.1002/2014JB011503 (2015).
24. Singhroha, S., Bünz, S., Plaza-Faverola, A. & Chand, S. Detection of gas hydrates in faults using azimuthal seismic velocity analysis, Vestnesa Ridge, W-Svalbard Margin. *J. Geophys. Res. Solid Earth.* **125**, e2019JB017949. https://doi.org/10.1029/2019JB017949 (2020).
25. Guerin, G., Goldberg, D. & Meltser, A. Characterization of in situ elastic properties of gas hydrate-bearing sediments on the Blake Ridge. *J. Geophys. Res.* **104**(B8), 17781–17795 (1999).
26. Jakobsen, M., Hudson, J. A., Minshull, T. A. & Singh, S. C. Elastic properties of hydrate-bearing sediments using effective medium theory. *J. Geophys. Res.* **105**(B1), 561–577 (2000).
27. Lee, J. Y., Francisca, F. M., Santamarina, J. C. & Ruppel, C. Parametric study of the physical properties of hydrate-bearing sand, silt, and clay sediments: 2. Small-strain mechanical properties. *J. Geophys. Res.* **15**, B11105. https://doi.org/10.1029/2009JB006670 (2010).
28. Chabert, A. *et al.* Characterization of a stratigraphically constrained gas hydrate system along the western continental margin of Svalbard from ocean bottom seismometer data. *J. Geophys. Res.* **116**, B12102. https://doi.org/10.1029/2011JB008211 (2011).
29. Wang, X. J., Hutchinson, D. R., Wu, S. G., Yang, S. X. & Guo, Y. Q. Elevated gas hydrate saturation within silt and silty clay sediments in the Shenhu area, South China Sea. *J. Geophys. Res.* **116**, B05102. https://doi.org/10.1029/2010JB007944 (2011).
30. Cook, A. E. & Tost, B. C. Geophysical signatures for low porosity can mimic natural gas hydrate: An example from Alaminos Canyon, Gulf of Mexico. *J. Geophys. Res. Solid Earth.* **119**, 7458–7472. https://doi.org/10.1002/2014JB011342 (2014).
31. Goswami, B. K. *et al.* A joint electromagnetic and seismic study of an active pockmark within the hydrate stability field at the Vestnesa Ridge, West Svalbard margin. *J. Geophys. Res. Solid Earth.* **120**, 6797–6822. https://doi.org/10.1002/2015JB012344 (2015).
32. Lee, J. Y., Santamarina, J. C. & Ruppe, C. Parametric study of the physical properties of hydrate-bearing sand, silt, and clay sediments: 1. Electromagnetic properties. *J. Geophys. Res.* **115**, B11104. https://doi.org/10.1029/2009JB006669 (2010).
33. Bellefleur, G., Riedel, M., Brent, T., Wright, F. & Dallimore, S. R. Implication of seismic attenuation for gas hydrate resource characterization, Mallik, Mackenzie Delta, Canada. *J. Geophys. Res.* **112**, B10311. https://doi.org/10.1029/2007JB004976 (2007).
34. Xu, H. N., Li, L. Q. & Shu, H. The seismic reflecting characteristics of gas hydrate bearing strata and its possible distribution in the South China Sea. *Appl. Geophys.* **3**(1), 42–47 (2006) (**in Chinese with English abstract**).
35. Yuan, J. & Edwards, R. N. The assessment of marine gas hydrates through electrical remote sounding: Hydrate without a BSR. *Geophys. Res. Lett.* **27**, 2397–2400 (2000).
36. Schwalenberg, K., Rippe, D., Koch, S. & Scholl, C. Marine-controlled source electromagnetic study of methane seeps and gas hydrates at Opouawe Bank, Hikurangi Margin, New Zealand. *J. Geophys. Res. Solid Earth.* **122**, 3334–3350. https://doi.org/10.1002/2016JB013702 (2017).
37. Zhu, Y. H., Zhang, Y. Q., Wen, H. J., Lu, Z. Q. & Wang, P. K. Gas hydrates in the Qilian Mountain permafrost and their basic characteristics. *Acta Geoscientica Sinica.* **31**(1), 7–16 (2010).
38. Lu, Z. Q., Xue, X. H., Liao, Z. W. & Liu, H. Source rocks for gases from gas hydrate and their burial depth in the Qilian Mountain permafrost, Qinghai: Results from thermal stimulation. *Energy Fuels.* **27**(12), 7233–7244. https://doi.org/10.1021/ef4010797 (2013).
39. Fang, H. *et al.* Geophysical characteristics of gas hydrate in the Muli area, Qinghai province. *J. Nat. Gas Sci. Eng.* **37**, 539–550 (2017).
40. Lu, Z. Q. *et al.* Oil and gas indications at gas hydrate bearing intervals in the Qilian Mountain permafrost. *Geoscience* **27**(1), 231–239 (2013).
41. Wang, P. K., Zhu, Y. H., Lu, Z. Q., Guo, X. W. & Huang, X. Gas hydrate in the Qilian Mountain permafrost and its distribution characteristics. *Geol. Bull. China* **30**(12), 1839–1850 (2011).
42. Fu, J. H. & Zhou, L. F. Carboniferous -Jurassic stratigraphic provinces of the Southern Qilian Basin and their petro- geological features. *Northwest Geosci.* **19**(2), 47–54 (1998).
43. Fu, J. H. & Zhou, L. F. Triassic stratigraphic provinces of the Southern Qilian Basin and their petro-geological features. *Northwest Geosci.* **21**(2), 64–72 (2000).
44. Sun, Z. J. *et al.* Geochemical characteristics of the shallow soil above the Muli gas hydrate reservoir in the permafrost region of the Qilian Mountains, China. *J. Geochem. Explor.* **139**, 160–169. https://doi.org/10.1016/j.gexplo.2013.10.006 (2014).
45. Lu, Z. Q. *et al.* Gas source for gas hydrate and its significance in the Qilian Mountain permafrost, Qinghai. *Mar. Petrol. Geol.* **43**, 341–348. https://doi.org/10.1016/j.marpetgeo.2013.01.003 (2013).
46. Lin, Z. L. & Moysey, S. M. J. The dependence of electrical resistivity-saturation relationships on multiphase flow instability. *ISRN Geophys.* https://doi.org/10.5402/2012/270750 (2012).
47. Guo, X. W. & Zhu, Y. H. Well logging characteristics and evaluation of hydrates in Qilian Mountain permafrost. *Geol. Bull. China.* **30**(12), 1869–1873 (2011).
48. Hu, X. D. *et al.* Anqi Liu 1,2 and Kouamelan Serge Kouamelan, Evaluation of gas hydrate saturation by effective medium theory in shaly sands: A case study from the Qilian Mountain permafrost, China. *J. Geophys. Eng.* **16**, 215–228. https://doi.org/10.1093/jge/gxy018 (2019).
49. Xiao, K., Zou, C. C., Lu, Z. Q. & Deng, J. Z. Gas hydrate saturations estimated from pore-and fracture-filling gas hydrate reservoirs in the Qilian Mountain permafrost, China. *Sci. Rep.* **7**(1), 16258 (2017).
50. Di, Q. Y. & Wang, M. Y. Determining areas of leakage in the Da Ye Dam using multi-electrode resistivity. *Bull. Eng. Geol. Env.* **69**, 105–109 (2010).
51. Archie, G. E. The electrical resistivity log as an aid in determining some reservoir characteristics. *Trans. AIME.* **146**(1), 54–62. https://doi.org/10.2118/942054-G (1942).
52. Lee, M. W. & Collett, T. S. In-situ gas hydrate saturation estimated from various well logs at the Mount Elbert Gas Hydrate Stratigraphic Test Well, Alaska North Slope. *Mar. Petrol. Geol.* **28**(2), 439–449. https://doi.org/10.1016/j.marpetgeo.2009.06.007 (2011).
53. Seigel, H. O. Mathematical formulation and type curves for induced polarization. *Geophysics* **24**(3), 547–565. https://doi.org/10.1190/1.1438625 (1959).

Acknowledgements

The authors are thankful to the Hui Fang, Shun-Min Wang, and Da-Wei Yao from the Institute of Geophysical and Geochemical Exploration CAGS for their assistance during the field work. We also grateful to Professor Changchun Chou from China University of Geosciences for his guidance in the study of lithological characteristics of gas hydrate reservoirs.

Author contributions

Conceptualization, D.L.; methodology, D.L., software, D.L., C.-M.F. and R.W.; validation, Z.-X.W.; formal analysis, Q.-H.Z. and R.W.; investigation, D.L., Q.-H.Z., Z.-X.W. and R.W.; resources, Z.-X.W.; data curation, D.L. and Z.-X.W.; writing—original draft preparation, D.L. and C.-M.F.; writing—review and editing, D.L. and C.-M.F.; visualization, C.-M.F. and D.L.; supervision, Z.-X.W.; project administration, Z.-X.W.; funding acquisition, D.L. and Z.-X.W. All authors read and agreed to the published version of the manuscript.

Funding

This research was funded by the Scientific Instrument Developing Project of the Chinese Academy of Sciences (ZDZBGCH2018006) and the Strategic Priority Research Program of the Chinese Academy of Sciences (XDA14050300).

Competing interests

The authors declare no competing interests.

Additional information

Correspondence and requests for materials should be addressed to D.L.

Reprints and permissions information is available at www.nature.com/reprints.

Publisher's note Springer Nature remains neutral with regard to jurisdictional claims in published maps and institutional affiliations.

Open Access This article is licensed under a Creative Commons Attribution 4.0 International License, which permits use, sharing, adaptation, distribution and reproduction in any medium or format, as long as you give appropriate credit to the original author(s) and the source, provide a link to the Creative Commons licence, and indicate if changes were made. The images or other third party material in this article are included in the article's Creative Commons licence, unless indicated otherwise in a credit line to the material. If material is not included in the article's Creative Commons licence and your intended use is not permitted by statutory regulation or exceeds the permitted use, you will need to obtain permission directly from the copyright holder. To view a copy of this licence, visit http://creativecommons.org/licenses/by/4.0/.

© The Author(s) 2022